Using an Engineered Galvanic Redox System to Generate Positive Surface Potentials that Promote Osteogenic Functions

Yulong Zhang[†,‡], **Zhong Zheng**[*,§], **Mengliu Yu**[§,∥], **Chinyun Hsu**[§], **Emily A. Berthiaume**[⊥], **Hsinchuan Pan**[§], **Xinli Zhang**[§], **Adam Z. Stieg**[#], **Benjamin Wu**[†,‡], **Huiming Wang**[*,∥], **Kang Ting**[*,§,#], and **Chia Soo**[*,¶]

[†]Department of Bioengineering, University of California, Los Angeles, California 90095, United States

[‡]Department of Advanced Prosthodontics, University of California, Los Angeles, California 90095, United States

[§]Division of Growth and Development, Section of Orthodontics, School of Dentistry, University of California, Los Angeles, California 90095, United States

[⊥]David Geffen School of Medicine, University of California, Los Angeles, California 90095, United States

[#]California NanoSystems Institute, University of California, Los Angeles, California 90095, United States

[¶]Division of Plastic and Reconstructive Surgery and Department of Orthopaedic Surgery and the Orthopaedic Hospital Research Center, University of California, Los Angeles, California 90095, United States

[∥]The Affiliated Hospital of Stomatology, College of Medicine, Zhejiang University, Hangzhou, Zhejiang 310006, China

Abstract

[*]**Corresponding Authors:** zzheng@dentistry.ucla.edu. Phone: +1 310 206 5646., Fax: +1 310 206 7783 (Z.Z.). hmwang1960@hotmail.com. Phone: +86 872 368 93 (H.W.). kting@dentistry.ucla.edu Phone: +1 310 206 6305., Fax: +1 310 206 7783 (K.T.). bsoo@ucla.edu. Phone: +1 310 794 5479., Fax: +1 310 206 7783 (C.S.).

ORCID

Yulong Zhang: 0000-0003-3089-196X
Zhong Zheng: 0000-0002-4905-3563

Author Contributions

Y.Z and Z.Z. contributed equally to this project. Y.Z. and Z.Z. performed the conception and design of the study. Y.Z., Z.Z., M.Y., and C.H. performed materials preparation, in vitro and in vivo experiments, and statistical analysis. H.P. performed the μCT image generation. X.Z. and K.T. performed histological image analyses. Y.Z., Z.Z., M.Y., and E.A.B. wrote the manuscript. A.Z.S. and B.W. supervised the physiochemical analyses. Z.Z., H.W., K.T., and C.S. supervised the entire study, provided the financial support, and approved the manuscript.
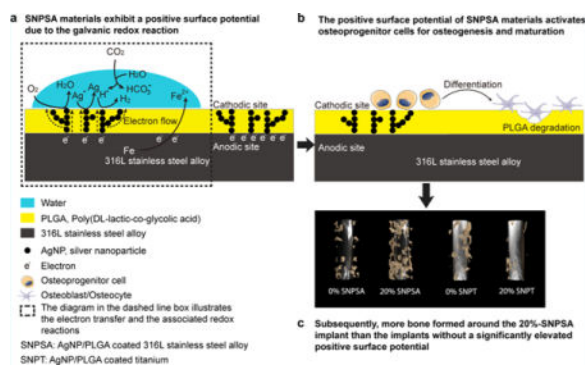
Successful osseointegration of orthopaedic and orthodontic implants is dependent on a competition between osteogenesis and bacterial contamination on the implant–tissue interface. Previously, by taking advantage of the highly interactive capabilities of silver nanoparticles (AgNPs), we effectively introduced an antimicrobial effect to metal implant materials using an AgNP/poly(DL-lactic-*co*-glycolic acid) (PLGA) coating. Although electrical forces have been shown to promote osteo-genesis, creating practical materials and devices capable of harnessing these forces to induce bone regeneration remains challenging. Here, we applied galvanic reduction–oxidation (redox) principles to engineer a nanoscale galvanic redox system between AgNPs and 316L stainless steel alloy (316L-SA). Characterized by scanning electron microscopy, energy-dispersive X-ray spectroscopy, atomic force microscopy, Kelvin probe force microscopy, and contact angle measurement, the surface properties of the yield AgNP/PLGA-coated 316L-SA (SNPSA) material presented a significantly increased positive surface potential, hydrophilicity, surface fractional polarity, and surface electron accepting/donating index. Importantly, in addition to its bactericidal property, SNPSA's surface demonstrated a novel osteogenic bioactivity by promoting peri-implant bone growth. This is the first report describing the conversion of a normally deleterious galvanic redox reaction into a biologically beneficial function on a biomedical metal material. Overall, this study details an innovative strategy to design multifunctional biomaterials using a controlled galvanic redox reaction, which has broad applications in material development and clinical practice.

Graphical abstract

a. SNPSA materials exhibit a positive surface potential due to the galvanic redox reaction

b. The positive surface potential of SNPSA materials activates osteoprogenitor cells for osteogenesis and maturation

- Water
- PLGA, Poly(DL-lactic-co-glycolic acid)
- 316L stainless steel alloy
- AgNP, silver nanoparticle
- e⁻ Electron
- Osteoprogenitor cell
- Osteoblast/Osteocyte
- [ ] The diagram in the dashed line box illustrates the electron transfer and the associated redox reactions

SNPSA: AgNP/PLGA coated 316L stainless steel alloy
SNPT: AgNP/PLGA coated titanium

c. Subsequently, more bone formed around the 20%-SNPSA implant than the implants without a significantly elevated positive surface potential

Keywords

1. INTRODUCTION

Despite progressive advancements in bone repair devices and techniques, approximately 6.68–14.4% of metal implant failures transpire because of insufficient bone growth and osseointegration.[1,2] The osseointegration quality of an implant relies on its ability to promote the differentiation and incorporation of host tissue cells while inhibiting the adhesion and proliferation of bacterial cells.[3] Therefore, it is imperative to design

orthopaedic and orthodontic implants that promote the osteogenesis of host tissue cells, but that also concurrently reduce microbial infections.[4,5]

To achieve this goal, processes that modify osteoinductive/osteoconductive material surface physiochemical properties, including the topography,[6] surface chemical property,[7] and electrical property,[8,9] have been investigated. For instance, electrical stimulation can promote bone regeneration.[10] Although the mechanism is not completely understood, collagen's piezoelectric property can generate a built-in electric field in the bone organic matrix,[11] which may activate the membrane receptors on osteoprogenitor cells to subsequently induce osteogenesis.[12] Beyond this inherent property, faradic products generated around cathodic sites during electrical stimulation also appear to contribute to bone regeneration.[13] The cations, such as Ca^{2+}, have the ability to rapidly deposit around the cathode, and anions, such as PO_4^{3-}, HPO_4^{2-} and OH^-, subsequently aggregate around the cations.[14] These depositions result in the formation of hydroxyapatite at the cathode, which promotes bone formation.[14] Attempts to induce osteogenesis with electric forces have used various methods, including direct electrical current,[7] capacitive coupling,[15] and inductive coupling.[9] However, the requirement of external devices to generate an electrical potential, invasive procedural methods, and high infection rates have considerably halted the application of electric stimulation in clinical settings.[16]

It is well-known that galvanic reduction–oxidation (redox) reactions occur on the surface of carbon steel in moist environments.[17–19] In this system, iron (Fe) acts as an anode, and the numerous interstitial doped surface carbon (C) atoms act as nanoscale cathodic sites. The electron flow from the anode (Fe) to the cathode (C) leads to an increased electron density and a higher negative electric potential on the anode than on the cathodic sites.[17–19] To harness this phenomenon, we sought to delicately engineer a similar nanoscale galvanic redox system that generates a positive surface potential (SP) on a biomedical metal material, and as a result, promotes bone growth and osseointegration of a metal implant.

Because of the large surface-to-mass ratio, silver nanoparticles (AgNPs) offer a greater active surface, higher solubility, and more chemical reactivity than nonnanoscale silver preparations. In comparison with nonnanoscale silver preparations, AgNPs have a greater release of oxidative Ag^+ and/or more partially oxidized AgNPs with chemisorbed (surface-bound) Ag(I).[20] Importantly, the electrode potential of the Ag particles significantly increases with a decrease in the particle size, especially when their size is reduced to nanoscale.[21] In addition, the immense active surface of the spherical AgNPs is critical for their antibacterial properties. Accumulating evidence demonstrates that AgNPs are effective, broad-spectrum antimicrobial agents that can be used in a wide range of doses with a diversity of materials to prevent and manage contamination and biofilm formation without toxicity.[22–26] Thus, AgNPs are desirable candidates for building a galvanic redox system with antimicrobial properties. Meanwhile, our previous studies have shown that poly(DL-lactic-*co*-glycolic acid) (PLGA) is an osteoconductive material capable of supporting a homogeneous distribution of AgNPs.[27] PLGA is used widely with other components of conducting polymers that permit electric current to pass.[28] Therefore, in this study, we coated AgNPs/PLGA on a biomedical metal, 316L stainless steel alloy (316L-SA), to empower a built-in electrical force on the surface of a metal implant. The central hypothesis

of this study is that AgNPs can function similarly to doped carbon atoms in carbon steel and initiate an electron flow from the substrate metal, 316L-SA, to the cathodic AgNPs in the coated surface, as the electron transfer is driven by the difference in electrode potential between the AgNPs and 316L-SA. As a result, we expected that the controlled galvanic redox reaction of the AgNP/PLGA-coated 316L-SA (SNPSA) would create a unique surface electrical property that could be regulated by the AgNP concentration to effectively stimulate local osteogenesis and osseointegration.

Although 316L-SA contains a 16–18.5% of chromium (by weight), and can form a passivation layer of chromium(III) oxide (Cr_2O_3) when exposed to oxygen, it is still more active than Ag, as shown in galvanic series charts delineating the relationships between different metals and their relative propensity to undergo redox reactions.[29,30] Thus, the different electrode potentials between 316L-SA and AgNPs make the galvanic redox reactions possible. In comparison, when titanium is exposed to oxygen, it immediately forms a stable, protective titanium oxide passivation layer on its surface that imparts a noble property. In this case, the electrode potential of the titanium substrate is close to that of Ag in the galvanic series,[29,30] and we inferred that there would be no such galvanic redox reaction between the AgNPs and the titanium substrate. To test our theory, titanium was used as a minimally reactive substrate to fabricate AgNP/PLGA-coated titanium (SNPT).

2. EXPERIMENTAL SECTION

2.1. Materials

Spherical AgNPs (20–40 nm, QSI-Nano Silver) were purchased from QuantumSphere, Inc. (Santa Ana, CA, United States). PLGA (lactic/glycolic = 85:15, inherent viscosity: 0.64 dL/g in chloroform) was purchased from Durect Co. (Pelham, AL, United States). Kirschner (K)-wires of 316L-SA and titanium (length: 70 mm, diameter: 0.8 mm) were purchased from Synthes, Inc. (Monument, CO, United States), while 316L-SA and titanium discs (diameter: 7 mm) were sliced from metal rods purchased at Stainless Supply (Monroe, NC, United States) using an electrical discharging machine at the University of California, Los Angeles (UCLA). All the other used chemicals were purchased from Sigma-Aldrich (St. Louis, MO, United States).

2.2. Fabrication of SNPSA and SNPT

We employed an electrospraying method to prepare the AgNP-coated metal materials. Spherical AgNPs were dispersed into PLGA/1,4-dioxane solution and then sprayed onto the metal materials. PLGA was used because it is both biodegradable and biocompatible and was approved by the U.S. Food and Drug Administration for clinical application. Briefly, metal K-wires and discs were fixed on a lathe mandrel and rotated at a speed of 3450 rpm. A total of 0.25 mL of AgNP/PLGA/1,4-dioxane solution was electrosprayed onto each K-wire surface over the course of 5 min. For each disc, a total of 0.05 mL of AgNP/PLGA/1,4-dioxane solution was electrosprayed onto the surface over the course of 1 min. The coated samples were placed in an oven at a temperature of 40 °C overnight and then transferred to a fume hood for 2 days of air-drying. After drying completely, the AgNP/PLGA-coated metal materials were hermetically sealed and stored at −20 °C until their use. Electro-spraying

resulted in higher AgNP proportions in the AgNP/PLGA layer without particle aggregation. The densities of the AgNP/PLGA layer were 0.263, 0.278, and 0.293 g/cm^3 at proportions of 0, 10, and 20% AgNP, respectively, and the densities of AgNPs in the coating surface were 0, 6.95, and 14.65 $\mu g/cm^2$ for 0, 10, and 20% AgNP/PLGA-coated metal materials, correspondingly.

2.3. Scanning Electron Microscopy and Energy-Dispersive X-ray Spectroscopy

Scanning electron microscopy (SEM) (Nova NanoSEM 230-D9064, FEI Company, Hillsboro, OR, United States) was used to evaluate the morphology of AgNP/PLGA-coated metal materials, while energy-dispersive X-ray spectroscopy (EDS) was documented simultaneously.[22,27] The surface atomic composition of silver (SAC_s) was analyzed based on the EDS measurement. The testing parameters were set to WD: 15 mm, primary electron energy: 10 keV, and process time: 5 s. For the EDS measurements, five samples were scanned for each group. Three different 80×40 μm areas were selected from each sample. Each area was scanned in quintuplicate.

2.4. Atomic Force Microscopy and Kelvin Probe Force Microscopy

The surface roughness (R_a; the arithmetic average of the absolute roughness profile values) of AgNP/PLGA-coated metal materials was assessed by topographic atomic force microscopy (AFM) imaging using the Bruker Dimension Icon Scanning Probe Microscope (Bruker Nano, Inc., Santa Barbara, CA, United States) in ambient conditions. Tapping (AM-AFM) mode imaging employed silicon cantilever probes (RTESP, Bruker Nano, Inc.) with nominal tip radii of 8 nm, spring constants of approximately 30 N/m, and resonant frequencies of 260–325 kHz. Height and phase images (2×2 μm) were acquired simultaneously using a 1 Hz scan rate. An automatic algorithm was used to flatten the images. R_a was quantified using the NanoScope Analysis V1.40 software package (Bruker Nano, Inc.).

Localized SPs of SNPSA and SNPT were characterized by Kelvin probe force microscopy (KPFM). KPFM imaging was conducted in the dual-pass amplitude modulated lift mode using Pt–Ir-coated silicon probes (SCM-PIT, Bruker Nano, Inc.) with nominal tip radii of 20 nm, spring constants of approximately 3 N/m, and resonant frequencies of 60–80 kHz. Co-localized topographic and SP images were acquired over 25×25 μm regions at a lift height of 100 nm. Reported values refer to the contact potential difference between the Pt–Ir tip and the surface. To minimize measurement variability, a single KPFM probe was used in the comparisons between SNPSA and SNPT, and five different locations on each sample surface from five samples in each group were analyzed.

2.5. Wettability and Surface Free Energy Characterization

Wettability and surface free energy values were obtained from contact angle (θ) measurements.[27,31–33] Advancing contact angles of multiple standard liquids (water-miscible dipolar liquids: formamide and ethylene glycol; water-immiscible non-polar liquid: diiodomethane) on the tested AgNP/PLGA-coated metal materials were measured using a contact angle analyzer (FPA125; First Ten Ångstroms, Portsmouth, VA, United States). The surface tension properties of these standard liquids are listed in Table S1.

The surface tension components of these liquids were analyzed based on the measured contact angles. On the basis of the Derjaguin, Landau, Verwey, and Overbeek model, the solid surface free energy (γ_S) can be divided into a nonpolar Lifshiz–van der Waals component (γ_S^{LW}) and a polar Lewis acid–base component (γ_S^{AB}), which is expressed as the geometric mean of the Lewis acid component (γ_S^+, electron acceptor) and the Lewis base component (γ_S^-, electron donor).[32] For a solid surface, the process can be described by eq 1. For solid/liquid interfacial interactions, γ_S, γ_S^{LW}, γ_S^{AB}, γ_S^+, and γ_S^- can be calculated according to eq 2.[32,33] In addition, the surface fractional polarity (SFP) was determined by γ_S^{AB}/γ_S, and the surface electron accepting/donating index (SEADI) was defined as the ratio of the electron-accepting parameter [$(\gamma_S^+)^{1/2}$] and electron-donating parameter [$(\gamma_S^-)^{1/2}$]. Five samples were tested for each group.

$$\gamma_S = \gamma_S^{LW} + \gamma_S^{AB} = \gamma_S^{LW} + 2 \cdot (\gamma_S^+ \cdot \gamma_S^-)^{1/2} \quad (1)$$

$$\gamma_L \cdot (1 + \cos\theta) = 2 \cdot (\gamma_S^{LW} \cdot \gamma_L^{LW})^{1/2} + 2 \cdot (\gamma_S^+ \cdot \gamma_L^+)^{1/2} + 2 \cdot (\gamma_S^- \cdot \gamma_L^-)^{1/2} \quad (2)$$

where γ_L, γ_L^{LW}, γ_L^+, and γ_L^- represent surface tension, nonpolar Lifshiz–van der Waals component, Lewis acid component, and Lewis base component of standard liquids, respectively.

2.6. Conditional Osteogenic Medium Treatment

Because of the dynamic and irreversible changes that surface properties of a material undergo during a successive osteogenesis process,[34] we used aconditional osteogenic medium (COM) treatment to mimic the physiology in which the biological and nonbiological components meet and interact on the implant surface. Transwell inserts were used to separate the cells and the coating surface during incubation (Figure S1) to preserve the physicochemical properties of the coating surface after COM treatment and eliminate damage to the coating matrix during the cell removal process mediated by trypsin digestion and mechanical scratching. Briefly, SNPSA and SNPT discs were incubated with 500 μL of osteogenic medium (α-minimum essential media supplied with 10% fetal bovine serum, 1% HT supplement, 100 unit/mL penicillin, 100 μg/mL streptomycin, 50 μg/mL ascorbic acid, and 10 mM β-glycerophosphate) at 37 °C for 6 days. To avoid the influence of direct cellular contact on surface morphology, 2×10^3 preosteoblastic MC3T3-E1 cells (subclone 4, ATCC CRL-2593; Manassas, VA, United States) were cultured on Matrigel (BD Biosciences, San Jose, CA, United States) precoated Transwell plates (Corning Inc., Corning, NY, United States).

2.7. MC3T3-E1 Cell Proliferation and Osteogenic Differentiation

MC3T3-E1 cells were seeded on SNPSA and SNPT metal discs at a density of 2×10^3 cells per disc and cultivated in the osteogenic medium in 24-well cell culture plates at 37 °C. Cell

proliferation on the AgNP/PLGA-coated metal discs was evaluated by the Vybrand MTT Cell Proliferation Assay Kit (Thermal Fisher Scientific, Canoga Park, CA, United States) after 9 days of cultivation. Alkaline phosphatase (ALP) activity, assessed by the 1-Step NBT/BCIP substrate solution (Thermal Fisher Scientific) at day 9, and the degree of mineralization, assessed by Alizarin Complexone staining (Thermal Fisher Scientific) at day 21, were used to quantify cellular differentiation. Images were taken by a fluorescence microscope (Olympus BX51, Tokyo). The mineralized area was defined as [(staining area/ total disc area) $\times$ 100] (%) using Image J software.

After 6 days of cultivation, total RNA or total protein was isolated by the RNeasy Mini Kit with DNase treatment (Qiagen, Valencia, CA, United States) or RIPA Buffer (Pierce Biotechnology, Rockford, IL, United States). One microgram of total RNA was used for reverse transcription with the iScript Reverse Transcription Supermix for quantitative real-time polymerase chain reaction (qRT-PCR) (Bio-Rad Laboratories, Hercules, CA, United States). qRT-PCR was performed with TaqMan Gene Expression Assays (Life Technologies) and SsoFast Probes Supermix with ROX (Bio-Rad Laboratories) on a 7300 Real-Time PCR system (Applied Biosystems Inc, Foster City, CA, United States). Osteogenic growth factors, such as transforming growth factor (Tgf)β1, bone morphogenetic protein (Bmp)2, and Bmp4, were analyzed for osteogenesis. Concomitant glyceraldehyde 3-phosphate dehydrogenase (Gapdh) was used as a housekeeping standard. Data analysis was achieved using the C_T method. Western blot analysis was performed to quantify the corresponding protein amounts. Anti-BMP2 (Abcam, Cambridge, MA, United States), anti-BMP4 (Abcam), anti-TGFβ1 (Santa Cruz Biotechnology, Santa Cruz, CA, United States), and GAPDH (Santa Cruz Biotechnology) primary antibodies were used at a dilution of 1:1000. All the experiments were repeated in triplicate.

2.8. Animal Model for in Vivo Bone Regeneration

All surgical procedures were approved by the UCLA Office of Animal Research Oversight (protocol #2012-120). A femoral intramedullary rod (FIR) model was used to assess the osteogenic ability of the metal materials that were utilized as intramedullary fixation devices in vivo.[35] Male Sprague-Dawley rats (12 weeks old) were randomly assigned to groups with different types of K-wire implants, with five rats in each treatment group. Briefly, the rats were anesthetized by isoflurane inhalation, the left femur was aseptically prepared, and an approach to the distal femur was made via a lateral knee arthrotomy. A 20-gauge needle was used to create an entry port into the proximal aspect of the femur medullary canal to ream the canal in preparation for placement of the intramedullary rod. A coated K-wire (2.7 cm in length) was inserted with the narrow portion first entering into the medullary canal, and then seated into the cortical bone in the distal aspect of the femur. The overlying muscle and fascia were closed with a 4–0 Vicryl absorbable suture. Following surgery, the animals were housed in separate cages and allowed to eat and drink ad libitum. Weight-bearing began immediately postoperatively, and the animals were monitored daily. Buprenorphine was administered for 2 days as an analgesic, but no antibiotics were administered postsurgery. The rats were euthanized by CO_2 treatment 8 weeks after implantation. No animals were excluded from the analysis.

2.9. 3D Microcomputed Tomography Scanning

Animals were euthanized 8 weeks after implantation. FIR model femurs were harvested and fixed in 4% paraformaldehyde for 48 h. The samples were scanned using high-resolution microcomputed tomography (μCT; SkyScan 1176, Bruker micro-CT N.V., Kontich, Belgium) at an image resolution of 18.0 μm (90 kV and 278 μA radiation sources with a 0.1 mm aluminum filter). 3D high-resolution images were generated by the CTAn software, following instructions provided by the manufacturer, and improved by Blender software. The ratio of bone volume (BV) to total volume (TV) was used to quantify bone tissue generation in vivo.

2.10. Histological Analysis

After μCT scanning, specimens were dehydrated with a graded solution of ethanol and cleared with xylenes. Specimens were then embedded in a fresh solution of methyl methacrylate, dibutyl phthalate, and Perkadox-16, and subsequently underwent polymerization. Specimens were cut as consecutive slides using Donath's technique and the EXAKT Cutting and Grinding System (EXAKT Technologies, Oklahoma City, OK, United States) and stained with Sanderson's Rapid Bone Stain. Van Gieson–Picrofuschsin was used as a counterstain. Specimens were imaged using an Olympus BX51 microscope. The area of mineralized bone was further quantified by Image J software.

2.11. Statistical Analysis

All statistical analyses were conducted in consultation with the UCLA Statistical Biomathematical Consulting Clinic. Statistical analyses were computed by OriginPro 8 (Origin Lab Corp., Northampton, MA, United States). Data are generally presented as mean ± the standard deviation and compared by one-way ANOVA and two sample t-tests. Mann–Whitney and Kruskal–Wallis ANOVA tests were used for nonparametric data. A Pearson's correlation coefficient was used for correlation tests. The p-values less than 0.05 were considered statistically significant.

3. RESULTS

3.1. Fabricating and Characterizing the Surfaces of SNPSA and SNPT Materials

The SNPSA and SNPT materials were fabricated by the same electrospraying method, and their graphical structures are illustrated in Figure 1. Employing electrochemical principles, we hypothesized that a nanoscale structure capable of enabling a galvanic redox reaction could be established on the SNPSA materials. The AgNPs embedded in the AgNP/PLGA matrix served as cathodic sites in the presence of moisture (Figure 1a,b), and 316L-SA was oxidized and served as an anode in the galvanic redox system (Figure 1a,b). Because of the noble metal property of the passive oxidized titanium surface, the titanium substrate and AgNPs cannot undergo redox reactions on the AgNP/PLGA-coated titanium (SNPT), even when the AgNP/PLGA-coatings of SNPT and SNPSA have the same composition and morphology (Figure 1c).

To test our hypothesis that the positive SP depends on the AgNP proportion in the PLGA layer, AgNP/PLGA matrices with different proportions of AgNPs were electrosprayed onto

the 316L-SA and titanium materials. EDS analysis identified Ag as an elemental component on the material surfaces (Table 1), which provides direct evidence that AgNPs were incorporated into the surfaces of the AgNP/PLGA-coated metal materials. SEM and AFM analyses revealed an even and smooth AgNP/PLGA layer on the 316L-SA and titanium without any distinct morphological differences (Figure 2a,b). This was further confirmed by R_a quantification (Figure 2c). The SP of the coating was analyzed by KPFM, which revealed the electronic homogeneity of the measured surface potentials of SNPSA and SNPT (Figure 2d). As we hypothesized, SNPSA exhibited significantly higher SP values when compared with the control (0% SNPSA without any encapsulated AgNPs), and the SP values are proportional to the AgNP content in the coating layer (Figure 2e). For example, the SP of 20%-SNPSA was 0.5 mV more positive than that of the 0%-SNPSA, while SNPT's corresponding SP value increase was less than 0.1 mV. Additionally, the SNPT samples that had the same AgNP proportions as the SNPSA samples retained lower SP values than their SNPSA counterparts (Figure 2e). These results demonstrate that the SP of AgNP/PLGA-coated metal material was dependent on the AgNP proportion in the AgNP/PLGA matrix, as well as the electrode potential of the metal substrates used.

The surface hydrophobic/hydrophilic properties of SNPSA and SNPT were compared by a contact angle measurement. The results showed that the surface contact angles of water-miscible dipolar liquids, formamide and ethylene glycol, were significantly decreased on both SNPSA and SNPT with increasing AgNP proportions in the AgNP/PLGA matrix, while the contact angles of water-immiscible nonpolar diiodo-methane were slightly increased (Table 2). These findings indicate that AgNP incorporation contributed to the hydrophilicity of the AgNP/PLGA-coated metal material surfaces. More importantly, the surface contact angles of water-miscible dipolar liquids on SNPSA were much smaller than the angles on SNPT when the same AgNP proportion was present in both of the respective surfaces (Table 2).

The calculated γ_S, γ_S^{LW}, γ_S^{AB}, γ_S^+, and γ_S^- of AgNP/PLGA-coated metal materials are summarized in Table 3. As expected, 0% SNPSA and 0% SNPT surfaces presented similar surface free energy values; however, the incorporation of AgNPs significantly increased γ_S^{AB}, which resulted in a higher SFP and SEADI in the AgNP/PLGA-coated metal materials, especially for the SNPSA (Table 3). These findings indicate that AgNPs play an important role in the proposed galvanic system. The SEADI of SNPSA was much higher than that of SNPT, which suggests that the SNPSA surface undergoes active electron transfer attributed to the electrochemical redox reaction. Moreover, the SEADI and SFP of SNPSA materials became significantly larger with increasing AgNP proportion, but the corresponding SNPT materials only experienced a limited increase in SEADI and SFP with increasing AgNP proportions (Table 3). These data strongly support our hypothesis that the nanoscale galvanic redox system is established on SNPSA, but not the surface of SNPT, as shown in Figure 1.

3.2. Surface Property Change after COM Treatment

After COM treatment, the sample surface was characterized by SEM, EDS, AFM, and contact angle measurement. Although SNPSA and SNPT presented similarly smooth surface morphologies before COM treatment (Figure 2a–c), the SNPSA surfaces had markedly more

heterogeneous morphologies after COM treatment, which is consistent with the increased R_a values that were obtained (Figure 3a–c). SNPSA had significantly higher R_a values than SNPT after COM treatment (Figure 3c). Additionally, the surface free energy (calculated based on contact angles in Table 4) indicates that the AgNP incorporation in the coating layer of the SNPSA materials led to significant increases in γ_S^{AB}, SFP, and SEADI values (Table 5). These results also showed that the SAC_s was significantly increased after COM treatment on the surface of SNPSA, but not on the surface of SNPT (Figure 3d,e). This suggests that more AgNPs were exposed on the surface of the SNPSA material after COM treatment, and thus, the polar γ_S^{AB} was much higher. This also increased the total γ_S and SFP values. A linear relationship between SFP and SAC_s was observed in both SNPSA and SNPT (Figure 3d, SNPSA: SFP = 3.47 × SAC_s + 1.66, Pearson's correlation coefficient = 0.964; SNPT: SFP = 1.11 × SAC_s + 1.70, Pearson's correlation coefficient = 0.974). The SNPSA had a much higher correlation slope than SNPT, which indicates that the SFP of SNPSA was more sensitive to the AgNP proportion in the AgNP/PLGA matrix. Importantly, the SEADI of SNPSA was linearly correlated to its SAC_s, but the SEADI of SNPT was not linearly correlated with its SAC_s (Figure 3e, SNPSA: SEADI = 0.0984 × SAC_s + 0.148, Pearson's correlation coefficient = 0.955; SNPT: SEADI = 0.0063 × SAC_s + 0.156, Pearson's correlation coefficient = 0.743).

3.3. Evaluating the Osteogenic Activities of SNPSA and SNPT in Vitro

To determine whether the SP generated on SNPSA surface presents any toxicity and promotes osteogenic differentiation in vitro, pre-osteoblastic MC3T3-E1 cells were cultured on SNPSA and SNPT discs. Previously, electric fields have been reported to induce the expression of osteogenic growth factors, including TGFβ1, BMP2, and BMP4, in osteoblastic cells.[36,37] In this study, after 6 days of cell cultivation, *Tgfβ1*, *Bmp2*, and *Bmp4* transcription levels of MC3T3-E1 cells grown on the cathode site of SNPSA materials were significantly increased in an AgNP-proportion-dependent manner, but there were no significant differences among MC3T3-E1 cells grown on SNPT (Figure 4a), as confirmed by the protein expression analysis (Figure 4b). The proliferation, ALP activity, and mineralization degree of MC3T3-E1 cells on SNPSA increased with the increasing AgNP proportion (Figure 4c,d). These findings are consistent with our previous report that there is no significant cytotoxicity observed against MC3T3-C1 cell growth on the tested SNPSA materials.[27] It is likely due to the fact that sustained release of [Ag(I)] controlled by the PLGA degradation does not impose huge toxicity to the cells, which could be another unanticipated benefit of the AgNP/PLGA composite. In contrast, AgNP incorporation did not affect proliferation or osteogenic differentiation of MC3T3-E1 cells seeded on SNPT. These results confirm that the SNPSA, with a positive SP on the AgNP/PLGA-coating layer, can induce MC3T3-E1 cell differentiation and maturation to achieve osteogenesis.

3.4. Evaluating the Bone Formation Capability of SNPSA and SNPT in Vivo

To confirm whether the SP generated on SNPSA could promote bone formation in vivo, SNPSA and SNPT implants were inserted into the femurs of rats to create an FIR model.[35] 3D μCT demonstrated that, after 8 weeks of implantation in the rat distal femoral cavity, more bone formed around 20% SNPSA implants than around non-Ag-coated metal materials

and 20% SNPT implants (Figure 5a). Also, the BV/TV ratio was significantly higher in the 20% SNPSA implants than that of the other tested implants (Figure 5b). However, there were no significant differences in the μCT images and BV/TV ratios between the 0% SNPSA and 0% SNPT implants. Histological evaluation permitted visualization of the mineralized bone with red coloring, and soft tissue with blue coloring. Consistent with the μCT results, there was more bone formation around the 20% SNPSA implants than around the 20% SNPT implants (Figure 5c,d). Interestingly, fibrotic soft tissues (blue staining) and cartilage-like tissues (purple staining) were only observed around the 20% SNPT implants (Figure 5c). These results suggest that SNPSA acquired through a galvanic redox system promoted bone formation in vitro and in vivo.

Histological analysis of 0% SNPSA and 0% and 20% SNPT showed a gap (a region of no staining) between the new bone and the implants because of the residual AgNP/PLGA layer, but almost no gap was observed in the 20% SNPSA implants (Figure 5c). This demonstrates that 20% SNPSA achieved earlier and more direct bone apposition on the implant surface compared to the other implants, which indicates a better capability for in vivo osseointegration. This phenomenon also demonstrated that the cathodic sites on the AgNP/ PLGA layer of the 20% SNPSA implants degraded faster because of the galvanic redox system, which is consistent with the finding that the SNPSA surface showed a significantly increased R_a after COM treatment in vitro. However, because the unique AgNP/PLGA matrix structure is a prerequisite for the galvanic redox system's formation and function, the galvanic redox reaction terminates when the AgNP/PLGA matrix is degraded. Thus, the transient existence of the engineered galvanic redox system does not lead to elevated corrosion of the 316L-SA. This was evidenced in the SEM images of the surface of the 316L-SA substrate from the 20% SNPSA implants after 8 weeks of implantation (Figure S2).

4. DISCUSSION

In this study, we documented a novel bioengineering strategy that generates built-in electrical forces on metal materials, which can facilitate osteogenesis and osseointegration in vitro and in vivo. In this strategy, nanoscale silver particles were embedded into a PLGA matrix and coated onto the metal surface. Because of the different electrode potentials between the substrate metal and AgNPs, the coating matrix modified the surface electron density and surface potential, and by doing so, altered the electrochemical property of the implant surface. This is the first report that describes the employment of a galvanic redox mechanism and nanotechnology to modify a metal surface, which introduces a novel bioactivity to a metal implant typically used for structural support.

Of the elements in the engineered redox pair on the surface of SNPSA implants, Fe, the major element (>62%) of 316L-SA, can be oxidized to Fe^{2+} and can release electrons that are transferred to the AgNP cathodes on the coating surface (Figure 1a). Meanwhile, Ag ions [Ag^+, or Ag(I)] can be reduced to Ag [Ag(0)] by accepting the electrons. AgNPs that connect to one another in the AgNP/PLGA matrix can serve as the electron conduction path between the anode and cathode sites. It should also be noted that carbon dioxide (CO_2) found in moisture (H_2O) can dissociate into bicarbonate (HCO_3^-) and hydrogen (H^+) ions.

The H$^+$ can also be generated by the degradation of PLGA. During redox reactions, H$^+$ can be reduced to H$_2$ on the AgNP cathodes in the AgNP/PLGA-coating layer of the SNPSA materials. The electrode reactions can occur according to the equations below (eq 3–5)

$$Fe - 2e^- \rightarrow Fe^{2+} \quad (3)$$

$$Ag^+ + e^- \rightarrow Ag \quad (4)$$

$$2H^+ + 2e^- \rightarrow H_2 \quad (5)$$
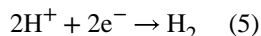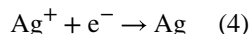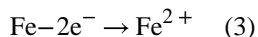
The high SPs found on the SNPSA surfaces by KPFM (Figure 2) supported our hypothesis that the nanoscale galvanic redox reactions occurred on the surface of SNPSA. In the nanoscale galvanic redox system fabricated to create SNPSA, the cathodic AgNP/PLGA layer showed a positive SP that was dependent on the proportion of AgNPs in the PLGA layer (Figure 2e). In contrast, the SNPT samples were not likely to develop the galvanic redox system because the electrode potential of the passive oxidized titanium surface is close to that of Ag in the galvanic series,[38,39] which impedes electron transfer from titanium to the AgNPs (Figure 1c). As a result, in comparison with SNPSA materials, SNPT materials had a less positive SP value (Figure 2).

The hydrophilicity of the SNPSA surface was significantly increased compared to that of SNPT (Tables 2 and 3), which can be attributed to the electrowetting effect.[40,41] The relationship of the wettability and the SP can be described qualitatively by the following equation (eq 6)[40]

$$\cos\theta(V) = \cos\theta(0) + \frac{1}{2} \times \frac{\varepsilon}{\delta \times \gamma_{LV}} V^2 \quad (6)$$

Here, V is the electrode potential in relation to the potential of the uncharged interface, $\theta(V)$ is the contact angle of the coating surface under the external electric field (after coating in this preparation), $\theta(0)$ is the contact angle without the external electric field (before coating in this preparation), δ is the thickness of the coating, ε is dielectric constant of the coating, and γ_{LV} is the interfacial tension between liquid/vapor phases. Therefore, the higher SP of SNPSA enhanced its surface hydrophilicity.

The cathodic reaction during the COM treatment is different from the cathodic reaction in a moist environment because of the high amount of water, the high ionic strength, and the physiological pH value (7.2–7.4). The predominant cathodic reactions during the COM treatment are described in the equations below (eqs 7 and 8)

$$2H_2O + 2e^- \rightarrow H_2 + 2OH^- \quad (7)$$

$$O_2 + 4H^+ + 4e^- \rightarrow 2H_2O \quad (8)$$
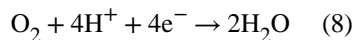
The generated OH^- promoted the degradation of PLGA, which led to a rough surface observed by SEM and AFM (Figure 3a–c), and more AgNP exposure on the coating surface. At the same time, the PLGA degradation released more H^+. Therefore, the cathodic reactions that are shown in eqs 4 and 5 cannot be completely excluded during the COM treatment because of the higher diffusion rate of H^+ than that of OH^- (9.311×10^{-5} vs 5.273×10^{-5} cm^2 s^{-1}).[42] Moreover, the SEADI values of SNPSA were much higher than those of SNPT, which indicate that the intensity of the electrochemical reaction on the surface of the SNPSA was much higher than the reaction on the SNPT. Collectively, these post-COM data further confirm our hypothesis that the nanoscale galvanic redox system formed on SNPSA, but not on SNPT.

Traditionally, galvanic reactions between dissimilar metals in direct contact have negative impacts on the surrounding tissue because the continuous electron flow generates elevated oxidation and corrosion of the implants.[43] This usually leads to poor implant performance and rejection.[43] However, by engineering a controlled galvanic redox reaction on the surface of the 316L-SA, we introduced a novel biological activity—osteogenesis—to a metal material by surface modification alone. Considering that stainless steel alloys comprise the majority of metals used for biomedical bone fixation, are stronger and less expensive than titanium, and account for more than half of the total biomedical metal market,[44] the newly fabricated SNPSA materials that hold bactericidal and osteogenic dual activities may exhibit particular benefits for orthopedic and orthodontic applications.[27] These enhanced bioactive orthopedic and orthodontic implants could be particularly applicable in scenarios that require elevated osseointegration and/or built-in electrostimulation. Therefore, this study describes an innovative and highly translational strategy to create osteogenic materials for bone regeneration and opens the possibility of developing materials with significantly improved biological functions.

In agreement with our hypothesis, the AgNP/PLGA coating on different metal substrates, which lead to different electrochemical properties, osteoinductivity, and consequent osseointegration, may also distinguish applications for the metal substrates in vivo. For example, SNPSA materials may be more suitable for permanent intramedullary fixation, especially in scenarios where a large volume of bone tissue is lost and osteoinductivity of the implants is required. Additionally, cases of permanent orthopedic and dental implantation in which osseointegration is crucial, such as joint replacement, prosthetic limbs, and teeth, may find SNPSA particularly useful because of its osteoinductive and antimicrobial properties. On the other hand, although titanium materials usually exhibit good biocompatibility and osseointegration because of the stable oxide layer on its surface,[45] our results demonstrate that introducing a thin AgNP/PLGA coating significantly improves the osseointegration

capacity of the less expensive 316L-SA compared to a titanium substrate. The titanium alloy may impart titanium dioxide nanoparticles, which have been reported to alter the viability and behavior of multiple bone-related cell types, increase bone resorption, and lead to clinical incidents of osteolysis, implant loosening, and joint pain.[46] Thus, for fractures without major tissue deficiencies, SNPT materials may be a more desirable choice for external fixation.

It is worth noting that, in general, safety remains a major concern for the clinical application of nanoscale materials, including AgNPs. AgNPs are generally recognized as safe in application because they have been widely used as an anti-bacterial material in health for decades.[47] Particularly, an AgNP-based material, SilvrSTAT, has been approved by the United States Food and Drug Administration (FDA),[26] which further encourages the bench-to-bed translation of AgNP-based materials. On the other hand, nanoparticles are capable to penetrate the lipid bilayer membranes and thus reach the cytoplasm.[48] Because of the short investigation period of nanomaterials, the nanoparticle–cell interactions, especially those relevant to the potential toxicity arising from absorption, distribution, metabolism, and excretion (ADME) of nanoparticles, have not been comprehensively assessed.[48] Further studies through a broad international, multidisciplinary collaboration are warranted to fully study the toxicity as well as the immunological influences of AgNP-based materials, especially their long-term effects, to further support their possible clinical application.

5. CONCLUSIONS

By characterizing the surfaces of the coated metal materials using SEM, EDS, AFM, KPFM, and contact angle measurement, we successfully demonstrated that delicately establishing a nanoscale galvanic redox system to alter the SP of a traditional biomaterial can induce novel bioactivities. For instance, by engineering a nanoscale galvanic redox system between AgNPs and 316L-SA, the AgNP/PLGA coating endowed bactericidal activities to the 316-SA and also introduced novel osteogenic stimulation properties into the system. This markedly advances the orthopedic and orthodontic applications of SNPSA materials. Importantly, the novel osteoinductivity was only present in the composite materials that could interact in a galvanic redox system but was not found in the individual components of the composite materials. From the example presented in this study, the AgNP/PLGA coating converted a normally deleterious galvanic redox reaction (e.g., rusting,[17,18] poor implant performance, and rejection[43]) on metal surfaces into a biological benefit that promoted peri-implant bone growth (Movie S1). The universal galvanic redox reaction can also be applied to other metallic materials, such as copper or zinc, and used in orthopedic, dental, and cardiovascular devices. From these findings, this study enables insight into both the generated electrical forces and potential applications of galvanic redox reactions in biomaterial engineering. We foresee that this study will offer a strong foundation for developing a new class of galvanic redox biomaterials that endow novel biological functions for use in regenerative medicine.

Supplementary Material

Refer to Web version on PubMed Central for supplementary material.

Acknowledgments

References

1. Wadhawan R, Brar AD, Singh M, Maniar A, Gaba N. Management of Ailing & Failing Implants: A Review. IOSR J Dent Med Sci. 2016; 15:101–109.

2. Mohajerani H, Roozbayani R, Taherian S, Tabrizi R. The Risk Factors in Early Failure of Dental Implants: A Retrospective Study. J Dent. 2017; 18:298–303.

3. Subbiahdoss G, Kuijer R, Grijpma DW, van der Mei HC, Busscher HJ. Microbial Biofilm Growth Vs. Tissue Integration: "The Race for the Surface" Experimentally Studied. Acta Biomater. 2009; 5:1399–1404. [PubMed: 19158003]

4. Raphel J, Holodniy M, Goodman SB, Heilshorn SC. Multifunctional Coatings to Simultaneously Promote Osseointegration and Prevent Infection of Orthopaedic Implants. Biomaterials. 2016; 84:301–314. [PubMed: 26851394]

5. Wood MR, Vermilyea SG. A Review of Selected Dental Literature on Evidence-Based Treatment Planning for Dental Implants: Report of the Committee on Research in Fixed Prosthodontics of the Academy of Fixed Prosthodontics. J Prosthet Dent. 2004; 92:447–462. [PubMed: 15523334]

6. Nadeem D, Smith C-A, Dalby MJ, Meek RMD, Lin S, Li G, Su B. Three-Dimensional Cap/Gelatin Lattice Scaffolds with Integrated Osteoinductive Surface Topographies for Bone Tissue Engineering. Biofabrication. 2015; 7:015005. [PubMed: 25562325]

7. Jeon H, Schmidt R, Barton JE, Hwang DJ, Gamble LJ, Castner DG, Grigoropoulos CP, Healy KE. Chemical Patterning of Ultrathin Polymer Films by Direct-Write Multiphoton Lithography. J Am Chem Soc. 2011; 133:6138–6141. [PubMed: 21452872]

8. Zhang W, Liu N, Shi H, Liu J, Shi L, Zhang B, Wang H, Ji J, Chu PK. Upregulation of Bmscs Osteogenesis by Positively-Charged Tertiary Amines on Polymeric Implants Via Charge/Inos Signaling Pathway. Sci Rep. 2015; 5:9369–9379. [PubMed: 25791957]

9. Ning C, Yu P, Zhu Y, Yao M, Zhu X, Wang X, Lin Z, Li W, Wang S, Tan G. Built-in Microscale Electrostatic Fields Induced by Anatase–Rutile-Phase Transition in Selective Areas Promote Osteogenesis. NPG Asia Mater. 2016; 8:e243. [PubMed: 27818718]

10. Kuzyk PRT, Schemitsch EH. The Science of Electrical Stimulation Therapy for Fracture Healing. Indian J Orthop. 2009; 43:127–131. [PubMed: 19838360]

11. Nair AK, Gautieri A, Chang S-W, Buehler MJ. Molecular Mechanics of Mineralized Collagen Fibrils in Bone. Nat Commun. 2013; 4:1724–1732. [PubMed: 23591891]

12. Black J, Baranowski TJ, Brighton CT. Electrochemical Aspects of Dc Stimulation of Osteogenesis. Bioelectrochem Bioenerg. 1984; 12:323–327.

13. Bodamyali T, Kanczler JM, Simon B, Blake DR, Stevens CR. Effect of Faradic Products on Direct Current-Stimulated Calvarial Organ Culture Calcium Levels. Biochem Biophys Res Commun. 1999; 264:657–661. [PubMed: 10543988]

14. Shirkhanzadeh M. Direct Formation of Nanophase Hydrox–apatite on Cathodically Polarized Electrodes. J Mater Sci: Mater Med. 1998; 9:67–72. [PubMed: 15348909]

15. Wang Z, Clark CC, Brighton CT. Up-Regulation of Bone Morphogenetic Proteins in Cultured Murine Bone Cells with Use of Specific Electric Fields. J Bone Jt Surg, Am Vol. 2006; 88:1053–1065.

16. Victoria G, Petrisor B, Drew B, Dick D. Bone Stimulation for Fracture Healing: Whats All the Fuss? Indian J Orthop. 2009; 43:117–120. [PubMed: 19838359]

17. Nishimura T, Katayama H, Noda K, Kodama T. Electrochemical Behavior of Rust Formed on Carbon Steel in a Wet/Dry Environment Containing Chloride Ions. Corrosion. 2000; 56:935–941.

18. Ghareba S, Omanovic S. Interaction of 12-Aminododecanoic Acid with a Carbon Steel Surface: Towards the Development of Green corrosion Inhibitors. Corros Sci. 2010; 52:2104–2113.

19. Alcántara J, de la Fuente D, Chico B, Simancas J, Díaz I, Morcillo M. Marine Atmospheric Corrosion of Carbon Steel: A Review. Materials. 2017; 10:406.

20. Lok C-N, Ho C-M, Chen R, He Q-Y, Yu W-Y, Sun H, Tam PK-H, Chiu J-F, Che C-M. Silver Nanoparticles: Partial Oxidation and Antibacterial Activities. J Biol Inorg Chem. 2007; 12:527–534. [PubMed: 17353996]

21. Yunfeng Y, Yongqiang X, Zixiang C, Miaozhi Z. Effect of Particle Size on Electrode Potential and Thermodynamics of Nanoparticles Electrode in Theory and Experiment. Electrochim Acta. 2014; 136:565–571.

22. Zheng Z, Yin W, Zara JN, Li W, Kwak J, Mamidi R, Lee M, Siu RK, Ngo R, Wang J, Carpenter D, Zhang X, Wu B, Ting K, Soo C. The Use of BMP-2 Coupled – Nanosilver-PLGA Composite Grafts to Induce Bone Repair in Grossly Infected Segmental Defects. Biomaterials. 2010; 31:9293–9300. [PubMed: 20864167]

23. Alt V, Bechert T, Steinrücke P, Wagener M, Seidel P, Dingeldein E, Domann E, Schnettler R. An in Vitro Assessment of the Antibacterial Properties and Cytotoxicity of Nanoparticulate Silver Bone Cement. Biomaterials. 2004; 25:4383–4391. [PubMed: 15046929]

24. Zhang S, Guo Y, Dong Y, Wu Y, Cheng L, Wang Y, Xing M, Yuan Q. A Novel Nanosilver/Nanosilica Hydrogel for Bone Regeneration in Infected Bone Defects. ACS Appl Mater Interfaces. 2016; 8:13242–13250. [PubMed: 27167643]

25. Jeong SH, Hwang YH, Yi SC. Antibacterial Properties of Padded Pp/Pe Nonwovens Incorporating Nano-Sized Silver Colloids. J Mater Sci. 2005; 40:5413–5418.

26. Lullove EJ, Brent Bernstein D. Use of Silvrstat in Lower Extremity Wounds: A Two Center Case Series. J Diabetes Complications. 2015; 7:13–16.

27. Liu Y, Zheng Z, Zara JN, Hsu C, Soofer DE, Lee KS, Siu RK, Miller LS, Zhang X, Carpenter D, Wang C, Ting K, Soo C. The Antimicrobial and Osteoinductive Properties of Silver Nanoparticle/Poly (DL-Lactic-Co-Glycolic Acid)-Coated Stainless Steel. Biomaterials. 2012; 33:8745–8756. [PubMed: 22959466]

28. Abidian MR, Kim D-H, Martin DC. Conducting-Polymer Nanotubes for Controlled Drug Release. Adv Mater. 2006; 18:405–409. [PubMed: 21552389]

29. Davis, JR. Corrosion: Understanding the Basics. ASM International; 2000.

30. Kadry S. Corrosion Analysis of Stainless Steel. Eur J Sci Res. 2008; 22:508–516.

31. Zheng Z, Bei F-F, Tian H-L, Chen G-Q. Effects of Crystallization of Polyhydroxyalkanoate Blend on Surface Physicochemical Properties and Interactions with Rabbit Articular Cartilage Chondrocytes. Biomaterials. 2005; 26:3537–3548. [PubMed: 15621244]

32. Mittal, KL. Contact Angle, Wettability and Adhesion. CRC Press; Boca Raton: 2009.

33. van Oss CJ, Chaudhury MK, Good RJ. Interfacial Lifshitz-Van Der Waals and Polar Interactions in Macroscopic Systems. Chem Rev. 1988; 88:927–941.

34. Hazan R, Brener R, Oron U. Bone Growth to Metal Implants Is Regulated by Their Surface Chemical Properties. Biomaterials. 1993; 14:570–574. [PubMed: 8399947]

35. Morandi M, Banka T, Gaiarsa GP, Guthrie ST, Khalil J, Hoegler J, Lindeque BG. Intramedullary Nailing of Tibial Fractures: Review of Surgical Techniques and Description of a Percutaneous Lateral Suprapatellar Approach. Orthopedics. 2010; 33:172–179. [PubMed: 20205366]

36. Zhuang H, Wang W, Seldes RM, Tahernia AD, Fan H, Brighton CT. Electrical Stimulation Induces the Level of TGF-β1 mRNA in Osteoblastic Cells by a Mechanism Involving Calcium/Calmodulin Pathway. Biochem Biophys Res Commun. 1997; 237:225–229. [PubMed: 9268690]

37. Bodamyali T, Bhatt B, Hughes FJ, Winrow VR, Kanczler JM, Simon B, Abbott J, Blake DR, Stevens CR. Pulsed Electromagnetic Fields Simultaneously Induce Osteogenesis and Upregulate Transcription of Bone Morphogenetic Proteins 2 and 4 in Rat Osteoblasts in Vitro. Biochem Biophys Res Commun. 1998; 250:458–461. [PubMed: 9753652]

38. LaQue, FL. Marine Corrosion: Causes and Prevention. Wiley; Hoboken, NJ: 1975.

39. Forman, CM., Verchot, EA. Practical Galvanic Series. Defense Technical Information Center; Fort Belvoir: 1967.

40. Welters WJJ, Fokkink LGJ. Fast Electrically Switchable Capillary Effects. Langmuir. 1998; 14:1535–1538.

41. Aronov D, Rosenman G, Karlov A, Shashkin A. Wettability Patterning of Hydroxyapatite Nanobioceramics Induced by Surface Potential Modification. Appl Phys Lett. 2006; 88:163902.

42. Guseva O, Schmutz P, Suter T, von Trzebiatowski O. Modelling of Anodic Dissolution of Pure Aluminium in Sodium Chloride. Electrochim Acta. 2009; 54:4514–4524.

43. Gittens RA, Olivares-Navarrete R, Tannenbaum R, Boyan BD, Schwartz Z. Electrical Implications of Corrosion for Osseointegration of Titanium Implants. J Dent Res. 2011; 90:1389–1397. [PubMed: 21555775]

44. Global Biomedical Metal Market. 3rd. Acmite Market Intelligence; Ratingen, Germany: 2014.

45. Tschernitschek H, Borchers L, Geurtsen W. Nonalloyed Titanium as a Bioinert Metal–a Review. Quintessence Int. 2005; 36:523–530. [PubMed: 15997933]

46. Yao JJ, Lewallen EA, Trousdale WH, Xu W, Thaler R, Salib CG, Reina N, Abdel MP, Lewallen DG, van Wijnen AJ. Local Cellular Responses to Titanium Dioxide from Orthopedic Implants. Biores. BioRes Open Access. 2017; 6:94–103. [PubMed: 29034133]

47. Chaloupka K, Malam Y, Seifalian AM. Nanosilver as a New Generation of Nanoproduct in Biomedical Applications. Trends Biotechnol. 2010; 28:580–588. [PubMed: 20724010]

48. Contini C, Schneemilch M, Gaisford S, Quirke N. Nanoparticle-Membrane Interactions. J Exp Nanosci. 2018; 13:62–81.
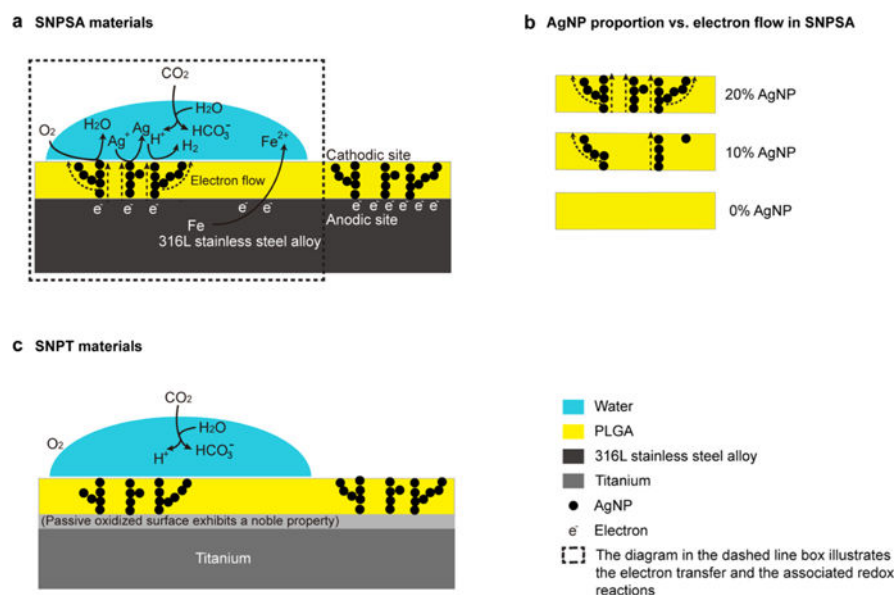
Figure 1.
Illustrations of the nanoscale galvanic redox system in the AgNP/PLGA-coated matrix on the surface of metal materials. (a) Positive SP of the AgNP/PLGA-coated 316L-SA (SNPSA) was generated by galvanic redox reactions, in which the iron (Fe) in 316L-SA was oxidized to Fe^{2+}, and the released electrons (e^-) were transferred to the AgNP cathodes. Meanwhile, the H^+, Ag^+, and O_2 were reduced at SNPSA's cathodic sites. A positive SP and the corresponding electric field were established around the cathodic sites. (b) Electron flow positively correlated with the AgNP proportion in the PLGA layer. In comparison to the 10% AgNP surfaces, the 20% AgNP surfaces had more AgNPs that were connected together to form electron-conducting paths. This leads to a greater electron flow and resulted in both higher SP and osteogenic ability. (c) There was no electron transfer from titanium to the AgNP surface because of the noble metal property of the titanium surface, and thus no nanoscale galvanic redox reactions occurred on the SNPT material.
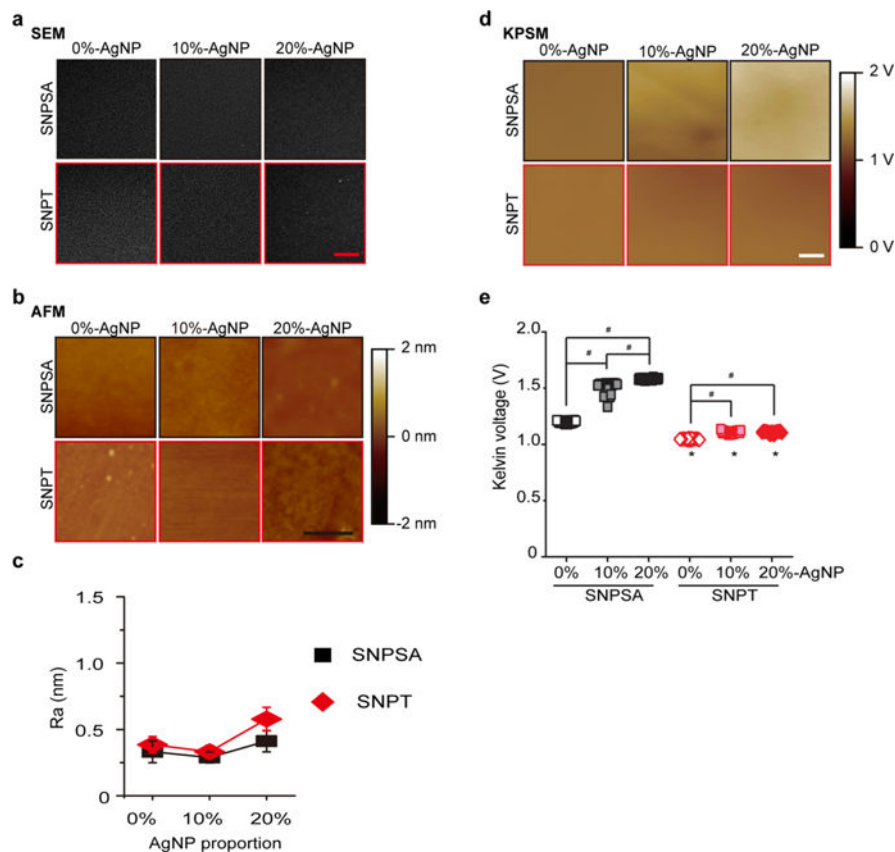
Figure 2.
SNPSA and SNPT surface morphologies and surface potentials. (a) SEM demonstrated an even, smooth AgNP/PLGA coating on SNPSA and SNPT with increasing AgNP proportions (0, 10, and 20%) in the coating layer. Scale bar: 20 μm. (b) AFM images confirmed that a homogeneous AgNP/PLGA matrix layer was generated on both the 316L-SA and titanium materials. Scale bar: 1 μm. (c) Measurements of surface roughness (R_a) show that there were no statistical differences between SNPSA and SNPT materials with the same AgNP proportions ($N = 3$). (d) KPFM documented the SPs of SNPSA and SNPT. Scale bar: 5 μm. (e) SP was quantified by analyzing a variety of different locations ($N = 29$). SNPSA had an increased SP, while no significant change in SNPT's SP was detected, even with an increasing AgNP proportion. Mann–Whitney analyses were used to detect statistical differences. [#]($p < 0.05$), significant difference resulting from different AgNP proportions; *($p < 0.05$), significant difference between SNPT and SNPSA with the same AgNP proportions.
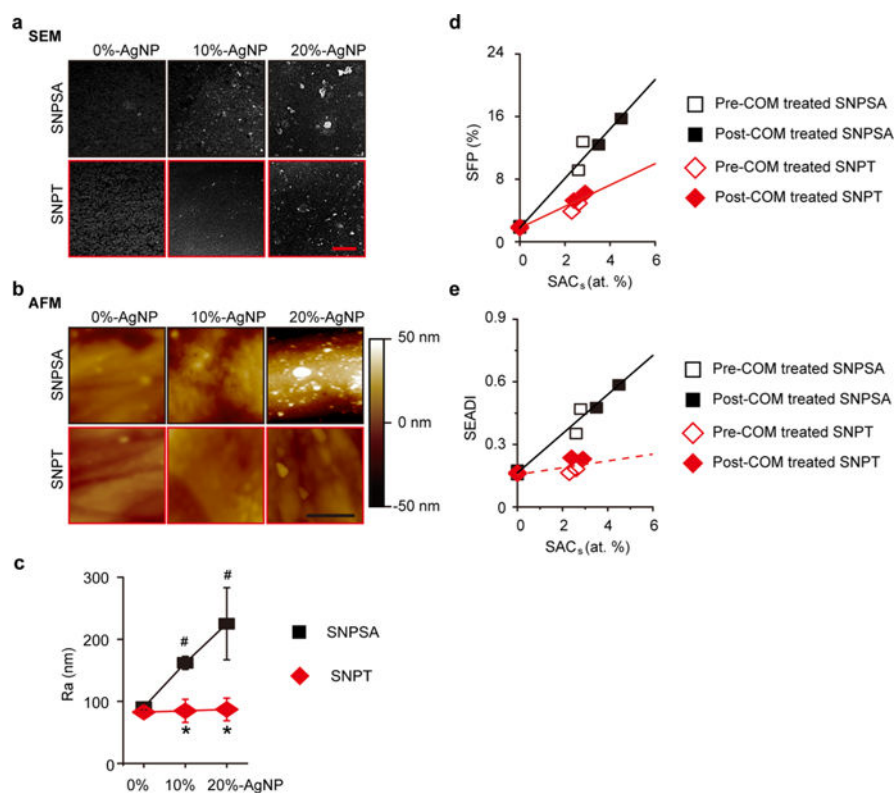
Figure 3.

Surface morphologies and properties of SNPSA and SNPT after COM treatment. (a,b) 6 days after COM treatment, SEM and AFM images showed that the SNPSA surfaces presented markedly heterogeneous morphologies with increasing AgNP proportions (0, 10, and 20%), while the SNPT surfaces did not show a significant change after COM treatment. Scale bar in a: 20 μm. Scale bar in b: 1 μm. (c) Surface roughness (R_a) measurement showed a significant difference in the surface morphology between SNPSA and SNPT at various AgNP proportions (0, 10, and 20%) after COM treatment. (d) Linear relationship between SFP and SAC_s was observed in both SNPSA and SNPT at various AgNP proportions (0, 10, and 20%) (SNPSA/SFP = $3.47 \times SAC_s + 1.66$, Pearson's correlation coefficient = 0.964; SNPT/SFP = $1.11 \times SAC_s + 1.70$, Pearson's correlation coefficient = 0.974). (e) Linear relationship between SEADI and SAC_s was observed in SNPSA (0, 10, and 20%) (SEADI = $0.0984 \times SAC_s + 0.148$, Pearson's correlation coefficient = 0.955), but not between the SEADI and SAC_s of SNPT (0, 10, and 20%) (SEADI = $0.0063 \times SAC_s + 0.156$, Pearson's correlation coefficient = 0.743). SNPSA's higher slope suggests that the Ag content on the surface had a significant effect on SNPSA's surface property because of the galvanic redox system in the coating layer. One-way ANOVA and two sample t-tests were used to detect statistical differences ($N = 3$). #($p < 0.05$), significant difference in comparison with 0% SNPSA; *($p < 0.05$), significant difference between SNPT and SNPSA with the same AgNP proportions.
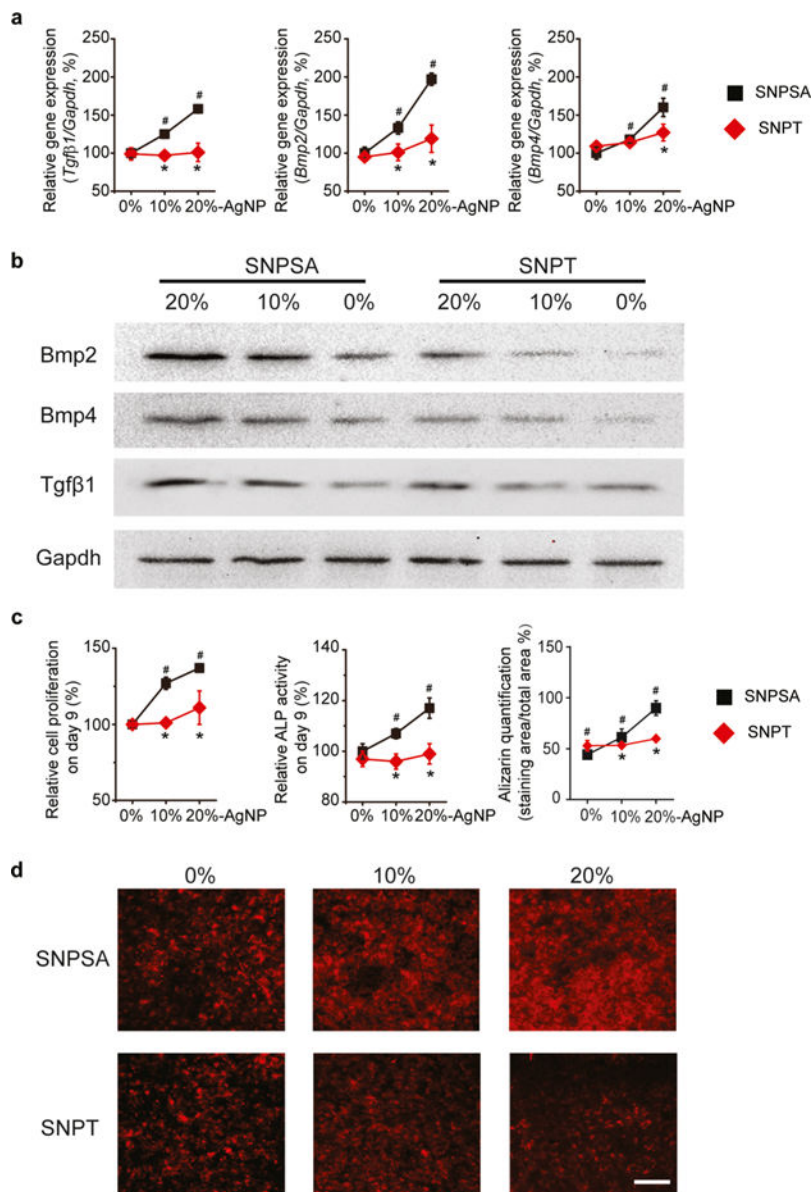
Figure 4.
Osteogenic ability of SNPSA and SNPT in vitro with different AgNP proportions (0, 10, and 20%). (a) After 6 days of cultivation, MC3T3-E1 cells grown on SNPSA had significantly increased transcription levels of *Tgfβ1*, *Bmp2*, *Bmp4*, and *Gapdh* in an AgNP-proportion-dependent manner. (b) Corresponding protein amounts were determined by western blot. (c) Growth and osteogenic differentiation of MC3T3-E1 cells on SNPSA and SNPT were determined by cell proliferation (day 9), ALP activity (day 9), and terminal mineralization (day 21). (d) MC3T3-E1 cells with alizarin complexone staining at day 21. Scale bar: 100 μm. Data were normalized to 0% SNPSA [$N = 3$ (a,d) or 6 (c)]. Kruskal–Wallis and Mann–Whitney analyses were used to detect statistical differences. [#]($p < 0.05$), significant difference in comparison with 0% SNPSA; *($p < 0.05$), significant difference between SNPT and SNPSA with the same AgNP proportions.
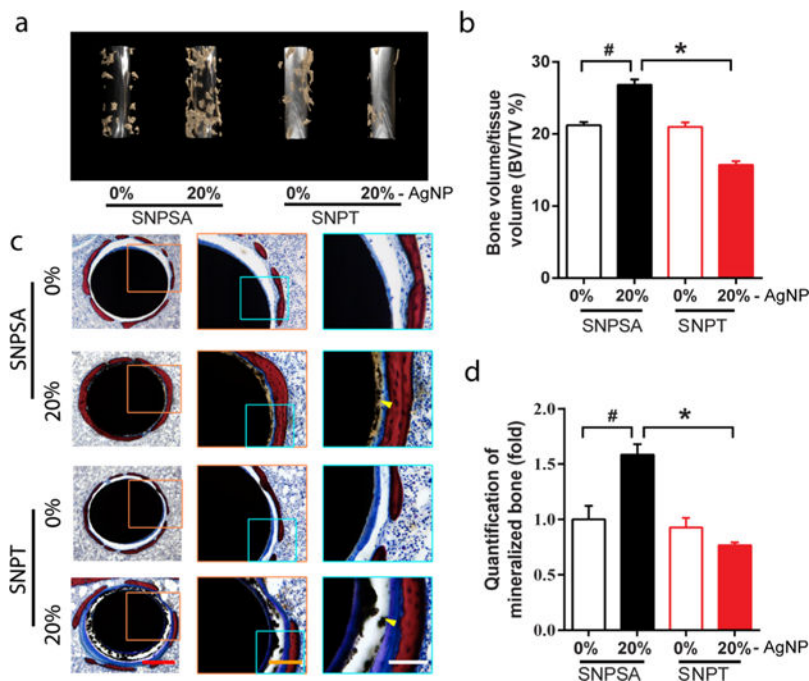
Figure 5.
In vivo osteogenic effects of SNPSA and SNPT in a rat FIR model. (a) 3D μCT reconstruction images of new bone formation in rat FIR cavities around 0% and 20% SNPSA and SNPT 8 weeks after implantation. More bone formed around 20% SNPSA than other tested materials. (b) Ratios of BV to TV (BV/TV) between SNPSA and SNPT were quantified. 20% SNPSA with the galvanic redox reaction showed significantly higher BV/TV when compared to the other groups. (c) Histological cross-section images of SNPSA and SNPT implants stained by Sanderson's rapid bone staining showed more mineralized bone (red staining) around the 20% SNPSA implants. More fibrotic soft tissue (blue staining) and cartilage-like tissue (purple staining) were observed around the 20% SNPT implants. Yellow arrows indicate the AgNP aggregation (black dots). Scale bar: 400 μm (red), 200 μm (orange), 100 μm (white). (d) Quantification analysis of the SNPSA and SNPT implant histological images ($N = 5$). Kruskal–Wallis and Mann–Whitney analyses were used to detect statistical differences. [#]($p < 0.05$), significant difference in comparison with 0% SNPSA; *($p < 0.05$), significant difference between SNPT and SNPSA at the same AgNP proportions.

Table 1

EDS Determination of SNPSA and SNPT Surface Atomic Compositions

metal material	AgNP proportion (%)	O atom (%)[a]	C atom (%)[a]	Ag atom (%)[a]
SNPSA	0	38.7 ± 0.4	61.3 ± 0.4	
	10	38.1 ± 0.1	59.3 ± 0.1	2.6 ± 0.1
	20	36.8 ± 0.4	60.4 ± 0.5	2.8 ± 0.1
SNPT	0	38.6 ± 0.2	61.4 ± 0.2	
	10	37.9 ± 0.6	59.8 ± 0.9	2.3 ± 0.4
	20	36.6 ± 0.1	60.8 ± 0.2	2.6 ± 0.2

[a]Data are shown as the mean ± standard deviation ($N = 10$).

Table 2

Surface Contact Angles of SNPSA and SNPT at 20°C

coated metal materials	AgNP proportion (%)	contact angle (Θ)[a]		
		formamide	ethyleneglycol	diiodomethane
SNPSA	0	49.1 ± 0.3	42.9 ± 0.4	43.6 ± 0.2
	10	31.6 ± 0.3	18.3 ± 0.4	44.7 ± 0.1
	20	28.9 ± 0.2	11.5 ± 0.2	45.8 ± 0.4
SNPT	0	49.8 ± 0.4	43.7 ± 0.1	43.5 ± 0.1
	10	36.9 ± 0.1	27.6 ± 0.2	44.2 ± 0.2
	20	34.3 ± 0.1	23.7 ± 0.3	45.0 ± 0.2

[a]Data are shown as the mean ± standard deviation ($N = 6$).

Table 3

Surface Free Energy Components of SNPSA and SNPT at 20 °C[a]

metal material	AgNP proportion (%)	γ_S	γ_S^{LW}	γ_S^{AB}	γ_S^+	γ_S^-	SEP ($\gamma_S^{AB}/\gamma_S\%$)	SEADI $(\gamma_S^+)^{1/2} (\gamma_S^-)^{1/2}$
SNPSA	0	38.48	37.80	0.68	0.05	2.19	1.77	0.151
	10	40.78	37.06	3.72	0.66	5.28	9.13	0.354
	20	41.74	36.41	5.33	1.25	5.69	12.8	0.469
SNPT	0	38.45	37.78	0.67	0.05	2.04	1.74	0.157
	10	38.86	37.36	1.50	0.12	4.58	3.86	0.162
	20	38.84	36.94	1.91	0.17	5.22	4.92	0.180

[a]Notes: γ_S, solid surface free energy component; γ_S^{LW}, nonpolar Lifshiz–van der Waals component; γ_S^{AB}, polar Lewis acid–base component; γ_S^+, Lewis acid component, electron acceptor; γ_S^-, Lewis basic component, electron donor; SFP, surface fractional polarity; SEADI, surface electron accepting/donating index.

Table 4

Surface Contact Angles of SNPSA and SNPT after COM Treatment at 20 °C

coated metal materials	AgNP proportion (%)	contact angle (Θ)[a]		
		formamide	ethyleneglycol	diiodomethane
SNPSA	0	49.2 ± 0.5	43.0 ± 0.6	44.2 ± 0.6
	10	30.8 ± 0.4	15.7 ± 0.3	46.0 ± 0.5
	20	27.4 ± 0.5	3.6 ± 0.6	46.3 ± 0.5
SNPT	0	48.9 ± 0.3	42.7 ± 0.4	44.3 ± 0.4
	10	38.0 ± 0.4	28.7 ± 0.5	44.9 ± 0.2
	20	33.3 ± 0.6	21.8 ± 0.5	45.2 ± 0.3

[a]Data are shown as the mean $\pm$ standard deviation ($N = 6$).

Table 5

Surface Free Energy Components of SNPSA and SNPT after COM Treatment at 20 °C[a]

metal material	AgNP proportion (%)	γ_S	γ_S^{LW}	γ_S^{AB}	γ_S^+	γ_S^-	SEP ($\gamma_S^{AB}/\gamma_S\%$)	SEADI $(\gamma_S^+)^{1/2}(\gamma_S^-)^{1/2}$
SNPSA	0	38.16	37.38	0.78	0.07	2.22	2.04	0.178
	10	41.44	36.30	5.14	1.22	5.39	12.4	0.476
	20	42.83	36.09	6.74	1.97	5.76	15.7	0.585
SNPT	0	38.05	37.32	0.73	0.06	2.30	1.92	0.162
	10	39.03	36.97	2.06	0.24	4.36	5.28	0.235
	20	39.27	36.82	2.45	0.28	5.35	6.24	0.229

[a]Notes: γ_S, solid surface free energy component; γ_S^{LW}, nonpolar Lifshiz–van der Waals component; γ_S^{AB}, polar Lewis acid–base component; γ_S^+, Lewis acid component, electron acceptor; γ_S^-, Lewis basic component, electron donor; SFP, surface fractional polarity; SEADI, surface electron accepting/donating index.